Mesoporous $CuFe_2O_4$ Photoanodes for Solar Water Oxidation: Impact of Surface Morphology on the Photoelectrochemical Properties**

Marcus Einert[+],*[a] Arslan Waheed[+],[a] Dominik C. Moritz,[a] Stefan Lauterbach,[b] Anna Kundmann,[c] Sahar Daemi,[c] Helmut Schlaad,[d] Frank E. Osterloh,[c] and Jan P. Hofmann[a]

Abstract: Metal oxide-based photoelectrodes for solar water splitting often utilize nanostructures to increase the solid-liquid interface area. This reduces charge transport distances and increases the photocurrent for materials with short minority charge carrier diffusion lengths. While the merits of nanostructuring are well established, the effect of surface order on the photocurrent and carrier recombination has not yet received much attention in the literature. To evaluate the impact of pore ordering on the photoelectrochemical properties, mesoporous $CuFe_2O_4$ (CFO) thin film photoanodes were prepared by dip-coating and soft-templating. Here, the pore order and geometry can be controlled by addition of copolymer surfactants poly(ethylene oxide)-*block*-poly(propylene oxide)-*block*-poly(ethylene oxide) (Pluronic® F-127), polyisobutylene-*block*-poly(ethylene oxide) (PIB-PEO) and poly(ethylene-*co*-butylene)-*block*-poly(ethylene oxide) (Kraton liquid™-PEO, KLE). The non-ordered CFO showed the

highest photocurrent density of 0.2 mA/cm² at 1.3 V vs. RHE for sulfite oxidation, but the least photocurrent density for water oxidation. Conversely, the ordered CFO presented the best photoelectrochemical water oxidation performance. These differences can be understood on the basis of the high surface area, which promotes hole transfer to sulfite (a fast hole acceptor), but retards oxidation of water (a slow hole acceptor) due to electron-hole recombination at the defective surface. This interpretation is confirmed by intensity-modulated photocurrent (IMPS) and vibrating Kelvin probe surface photovoltage spectroscopy (VKP-SPS). The lowest surface recombination rate was observed for the ordered KLE-based mesoporous CFO, which retains spherical pore shapes at the surface resulting in fewer surface defects. Overall, this work shows that the photoelectrochemical energy conversion efficiency of copper ferrite thin films is not just controlled by the surface area, but also by surface order.

Introduction

In light of the fact that climate change accelerated rapidly over the last decades, it is of vital importance to decrease the emission of greenhouse gases drastically in order to ensure habitable conditions on earth.[1] Therefore, the transfer from fossil fuels to CO_2-neutral, renewable energy technologies is essential. Hydrogen is a fuel which contains energy in the form of stored electrons and can be generated in a direct way by semiconductor-assisted photoelectrochemical water

splitting.[2–5] The process was first demonstrated on TiO_2 electrodes in 1972.[6] Since then, numerous nanostructured inorganic materials have been extensively investigated as photoelectrodes in terms of tailoring the physicochemical properties in order to increase their solar-to-hydrogen conversion efficiencies.[7–9] The major requirements for photoelectrodes are good absorption in the visible spectrum of light, efficient charge carrier mobility, and sufficiently high photovoltages, but also non-toxicity and abundance of elements allowing the cost-effective production for industrial, large-scale application. In

[a] M. Einert,[+] A. Waheed,[+] D. C. Moritz, J. P. Hofmann
Department of Materials and Earth Sciences
Surface Science Laboratory
Technical University of Darmstadt
Otto-Bernd-Strasse 3, 63287 Darmstadt (Germany)
E-mail: meinert@surface.tu-darmstadt.de

[b] S. Lauterbach
Institute for Applied Geosciences
Geomaterial Science
Technical University of Darmstadt
Schnittspahnstrasse 9, 64287 Darmstadt (Germany)

[c] A. Kundmann, S. Daemi, F. E. Osterloh
Department of Chemistry
University of California
One Shields Avenue, Davis, CA 95616 (USA)

[d] H. Schlaad
Institute of Chemistry
University of Potsdam
Karl-Liebknecht-Strasse 24–25, 14476 Potsdam (Germany)

[+] These authors contributed equally to this work.

[**] A previous version of this manuscript has been deposited on a preprint server (https://doi.org/10.26434/chemrxiv-2022-txgvp).

🖥 Supporting information for this article is available on the WWW under https://doi.org/10.1002/chem.202300277

Chemistry–A European Journal

Research Article
doi.org/10.1002/chem.202300277

Chemistry
Europe
European Chemical
Societies Publishing

particular, copper and iron-based metal oxides have attracted the attention of materials scientists since this class of absorbers meets most of the required properties for efficient photo-electrochemical (PEC) water splitting.[10,11] Since none of the well-studied earth-abundant binary oxides, such as α-Fe_2O_3,[12,13] CuO,[14,15] and Cu_2O,[16,17] fulfil all requirements for efficient PEC water splitting yet, research has also focused on ternary oxides.[18] In particular, ferrite-based photoelectrodes were demonstrated to be good absorbers in the visible spectrum with suitable band edge positions for both solar hydrogen and oxygen production depending on their doping type.[10,19] Spinel ferrites, such as $MgFe_2O_4$,[20] $ZnFe_2O_4$,[21,22] $CuFe_2O_4$,[23,24] and $CaFe_2O_4$[25] have been stated to be promising photoelectrodes, despite performing much below their theoretical PEC performance, the reasons for which are partially unclear. $CuFe_2O_4$ (CFO) has been reported to show both n-type and p-type conductivity and thus is applicable as photoanode[23,26] and photocathode,[24,27] respectively. The best reported cathodic photocurrent density for PEC water splitting of solution-processed CFO has been found to be 0.5 mA/cm^2 at 1.6 V vs. RHE owing to very short hole diffusion lengths (4 nm) and slow charge transfer limiting the overall charge carrier collection.[10,26] Calculations for n-type $CuFe_2O_4$ result in a theoretical maximum photocurrent density of $\sim$8.5 mA/cm^2 corresponding to a solar-to-hydrogen conversion efficiency of $\sim$10%.[23] The yet low photocurrents and photovoltages indicate the need for further investigations in order to overcome these major drawbacks. Also, photodegradation is a frequently observed competitive reaction in metal oxides when the oxidation potential and reduction potential lie, from an energetic point of view, above the valence band maximum (for n-type) and below the conduction band minimum (for p-type).[28] If this applies, photogenerated electron-hole pairs are capable of oxidizing and reducing the semiconductor itself, a reaction often falsely interpreted and ascribed to hydrogen or oxygen evolution.[29] Besides, ferrites were further utilized as semiconducting component to form heterojunctions for efficient charge carrier separation and/or as protection layers.[19] Cots et al. reported on the formation of a CFO protection layer on CuO photocathodes with suitable band alignment for efficient charge transport,[30] whereas most CFO photocathodes were shown to be photo-stable only from seconds to a few minutes under cathodic conditions.[27] The data imply that controlling the ferrite structure by tailoring the synthetic parameters in order to fabricate nano-morphologies providing short charge carrier transport distances is mandatory since photo-corrosion is potentially prevented in this way. Therefore, the need for nanostructured ferrites readily available on conductive substrates is indicated.

Polymer templating of inorganic structures is such a synthetic strategy to fabricate nanosized materials. Brinker and others established the evaporation-induced self-assembly (EISA) process in the 1990's,[31] and since then, numerous metal oxides have been prepared as mesoporous thin films for distinct energy applications by soft-templating.[32–36] Depending on the selection of the block copolymer structure-directing agent, the degree of pore ordering, geometry, and connectivity in the

mesoporous network upon annealing can change significantly: ranging from periodically arranged and uniformly sized mesopores[32] to totally disordered mesoporous frameworks with a broad pore size distribution.[21] The collapse of the mesopore framework during calcination using commercially available polymer surfactants, such as from the Pluronic® family, is known to be due to the formation of insufficiently thick pore walls impeding the uniform nucleation and growth of the nanocrystals.[37–39] The diblock copolymer KLE, that is (poly(ethylene-co-butylene)-block-poly(ethylene oxide), KL stands for Kraton Liquid™ and E for poly(ethylene oxide)), has proven to have superior templating properties due to its high hydrophilic-hydrophobic contrast and high thermal stability.[40] KLE enables the development and growth of thick pore walls within the inorganic structure allowing the amorphous precursor framework to transform into a nanocrystalline phase with retention of the mesopore structure and periodicity. It has been utilized as a template for the direct synthesis of numerous large-mesopore spinel ferrites with the general formula XFe_2O_4 (X = Mg, Zn, Co, Ni, Cu) possessing repeating distances typically ranging from 15 to 20 nm.[41–45] Brezesinski et al. prepared highly ordered, KLE templated CFO thin films and characterized them as photocatalysts for organic dye degradation presenting strong absorption in the visible light spectrum and fast degradation rates.[41] When comparing KLE, polyisobutylene-block-poly(ethylene oxide) (PIB-PEO), and poly(ethylene oxide)-block-poly(propylene oxide)-block-poly(ethylene oxide) (Pluronic® F-127) as porogens in mesoporous $MgTa_2O_6$ powders for photocatalytic degradation of rhodamine B, Smarsly et al. found that KLE-templated samples showed the highest photoactivity, attributable to the preservation of concave mesopores better compensating thermally induced mismatches.[46] Kirchberg et al. investigated the influence of the mesopore geometry in $ZnFe_2O_4$ (ZFO) photoanodes on their PEC activity with the outcome that disordered mesoporous morphologies showed better performance.[21] The improved photoresponse of the non-ordered ZFO structures was attributed to the higher crystallinity when using Pluronic® F-127 as structure-directing agent. Importantly, no detailed studies are available up to now revealing the impact of the pore ordering and surface morphology in mesoporous metal oxide thin film electrodes on the photoelectrochemical properties, in terms of quantification of the charge carrier dynamics, such as the transfer and surface recombination rates. The precise evaluation of these parameters and their dependence on the surface morphology and degree of crystallinity is of great importance to understand the limiting factors of mesoporous materials applied as photoelectrodes for solar water splitting. Up to now, there is only one study available in literature reporting on the PEC performance of KLE-templated ferrites, which explores periodically ordered high-entropy spinel photoanodes.[47] Furthermore, Laberty-Robert et al. demonstrated for PIB-PEO templated ordered mesoporous WO_3 photoanodes that the PEC photoresponse of the mesostructured species was increased compared to dense WO_3 thin films. These data are supported by the work of Yagi et al. in which the high PEC water oxidation performance of small-sized mesoporous WO_3 photoanodes was assigned to both the high

Chemistry–A European Journal

Research Article
doi.org/10.1002/chem.202300277

Chemistry
Europe
European Chemical
Societies Publishing

surface area (158 m²/g) which offered a large amount of catalytically active oxidation sites and the shorter carrier diffusion length which was provided by the 4–6 nm sized pore walls.[48] In a follow-up study, the Yagi group was also able to prove that the increase of surface area and organization of the mesopore network, resulting in thicker pore walls and increased pore ordering in WO₃, gave an improvement of the visible-light-driven PEC water oxidation.[49] The current literature data on mesoporous metal oxides for PEC applications imperatively highlight the necessity for further characterization of charge carrier dynamics in the bulk as well as at the surface of mesostructured materials in order to understand the limiting performance factors. Knowledge about these parameters opens up the path toward synthetic optimization of tailored nanostructures of metal oxide photoelectrodes providing ideal electron-hole pair migration paths/lengths based on their specific charge carrier lifetimes.

Therefore, the scope of the present work is to identify the impact of pore geometry and ordering on the structural, electronic and photoelectrochemical properties of sol-gel derived, mesoporous $CuFe_2O_4$ thin films. Using the *block*-co-polymer KLE, ordered mesoporous CFO thin films were produced by the EISA process and were – to the best of our knowledge – for the first time investigated as photoanodes for solar water splitting. The key factors when discussing the photoelectrochemical performance were found to be in the overall surface area and in the concentration of surface (defect) states, which were analyzed and verified by differential scanning voltammetry (DSV), surface photovoltage spectroscopy (SPS), and Mott-Schottky data. The energy band diagram derived by XPS showed that the CFOs are capable of performing overall water splitting. The materials properties obtained by X-ray-based structural characterization methods were correlated to the photoelectrochemical performance and help to explain how the pore ordering impacts these relevant parameters.

Results and Discussion

Structural Characterization

The mesoporous CFO thin films were prepared via the well-known EISA process by dip-coating. For successful preparation of mesoporous CFO thin films, a low relative humidity between 12–16% upon dip-coating (in order to accelerate the evaporation of the organic solvents) and pre-stabilizing step at 300°C for 12 h in air were required in order to enhance the condensation reactions of the metal hydroxides and to stabilize the amorphous precursor network. After the stabilization step, the materials were heated with a fast heating rate to 600°C and held at this temperature for 10 min – both prerequisites to avoid collapse of the mesoporous framework, which can be considered a metastable phase. Three different block copolymers, namely Pluronic® F-127, PIB-PEO, and KLE, the respective samples referred in the following to CFO-F127, CFO-PIB, and CFO-KLE, have been used in order to modify the pore ordering and surface morphology of CFO thin films and to examine how

the photoelectrochemical properties are affected by the evolution of distinct mesoporous frameworks. To understand the (photo-) electrochemical processes, which occur at the surface of the (photo-) electrodes, it is important to investigate their surface structure and morphology in detail. Hence, scanning electron microscopy (SEM) and transmission electron microscopy (TEM) analysis were performed on CFO-KLE, CFO-PIB, and CFO-F127 samples, providing information about the surface morphology on the micro- and nanoscale. Figure 1 shows the SEM and TEM images of CFO thin films after calcination for 10 min at 600°C in air. At this temperature, the structure-directing agents/templates are known to be fully degraded and the initial hybrid amorphous network is fully transformed into an inorganic mesoporous framework.[50]

The samples prepared with Pluronic® F-127 as template (Figure 1A) possess a random distribution of pores with an average pore diameter of 12–18 nm and a wormlike surface morphology which is typical for such mesoporous metal oxide thin films.[21] PIB-based CFO thin films (Figure 1B) contain a partially ordered mesopore system where preservation of the pore walls is predominantly maintained in the network. These samples possess an average pore diameter of 16–22 nm. The reason for the random and partially ordered pore distribution has already been discussed for mesoporous $ZnFe_2O_4$ photoanodes and is due to the difference in thermostability of the two polymers upon calcination.[21] The observed surface structures are comparable to other PIB templated metal oxides, such as for titania[51] and indium doped tin oxide.[52] While the decomposition of Pluronic® F-127 was reported to start at 300°C, PIB-PEO and KLE do not decompose below 400°C. As a result, the decomposition of F-127-based micellar structures and the transition of the amorphous network (metal oxide precursors) into an inorganic nanoarchitecture occur within the same temperature range. Additionally, Pluronic® F-127 creates insufficiently thick pore walls. Both properties finally lead to a collapse of the initially ordered mesoporous framework. In contrast, the CFO-KLE films (Figure 1C) possess the highest degree of pore ordering with mesopores ranging between 15 nm to 20 nm in diameter. Figure 1C reveals that the ordered mesoporous surface network is preserved even after calcination at 600°C for 10 min. Besides its thermal stability, KLE is known to form highly ordered micelle structures *via* the EISA-process, creating composites with sufficiently thick pore walls allowing uniform growth of the crystalline domains during thermal treatment.[32,53] All CFO thin films were found to be crack-free even at the macroscopic scale (see Supporting Information Figure S1), underlining the successful formation of overall homogeneous CFO samples with reproducible morphologies.

Selected-area electron diffraction (SAED) patterns provide information on the crystallographic structure of the materials and help to assess the degree of crystallinity. The SAED patterns show diffraction signals of nanocrystalline structures, which can be indexed to the tetragonal spinel phase (JCPDS no. 034-0425). For further investigation of the crystallographic structure and crystallinity of the CFO thin films, grazing-incidence X-ray diffraction (GI-XRD) experiments were conducted (Figure 2A). The Bragg peaks in the diffraction patterns of all CFO samples
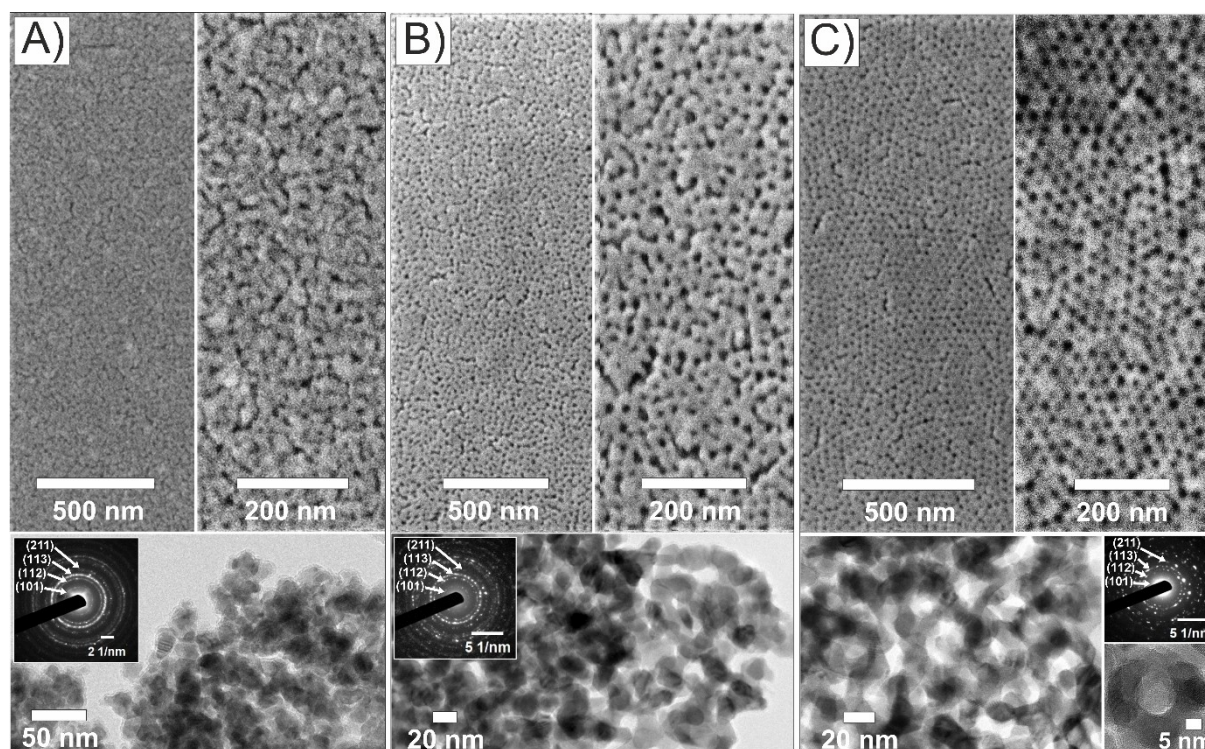
Chemistry–A European Journal

Research Article
doi.org/10.1002/chem.202300277

Chemistry Europe
European Chemical
Societies Publishing

Figure 1. SEM (upper pictures) and bright-field TEM (lower pictures) images of mesoporous CFO thin films calcined at 600 °C for 10 min using A) Pluronic® F-127, B) PIB-PEO, and C) KLE as structure-directing agents during sol-gel synthesis. SAED patterns from bulk areas including several crystallites were indexed consistently for the tetragonal spinel phase.

can be solely indexed to the tetragonal spinel phase and match well with the reference JCPDS no. 034-0425 (space group I $4_1/a$ m d) and further confirm the absence of any secondary phase formation. We note that CuO and α-Fe_2O_3 are thermodynamically stable phases, which are known to be potentially present as side phases for sol-gel derived $CuFe_2O_4$.[54]

Therefore, the mesoporous CFO thin films can be collectively considered as phase-pure, thus allowing direct comparison of their photoelectrochemical properties. The crystallite sizes have been calculated by using the Scherrer equation applied for the (101)-peaks. The nanocrystals were found to be in the range of 14–15 nm for all CFO samples, which is in good agreement with SEM and TEM data (Figures 1 and S2) and reveals that the structure-directing agent seems to have no influence on the final crystallite size. Due to nanosizing, commonly observed superposition and broadening of the diffraction peaks occur (Figure 2A).[55–58]

Since the surface area of any material determines the mass transport and the charge carrier exchange at its interface, it is of fundamental importance to investigate the electrochemical active surface area (ECSA). Therefore, the double-layer capacitance was determined from the corresponding differential cyclic scans (Figure S3) according to literature.[59] The C_{DL}, which directly correlates with the ECSA, was evaluated to be 0.195 mF/cm², 0.097 mF/cm², and 0.107 mF/cm² for CFO-F127, CFO-PIB, and CFO-KLE thin films, respectively.

These results indicate that the CFO-F127 samples possess the highest surface area. The impact of the surface area will be

discussed in more detail in the *Photoelectrochemical Characterization* section.

XPS was conducted to analyze the composition, chemical status, and electronic band diagram of the Pluronic® F-127, PIB-PEO and KLE templated CFO thin films. Figure S4A shows the XPS survey scan of each sample confirming the presence of all expected elements. In the high resolution XPS scans of the Cu 2p spectra, all photoemission peaks appear at a binding energy BE = 933.7 eV, which can be assigned to the $2p_{3/2}$ level and two satellite peaks present between 939 eV and 942 eV. Both are related to Cu cations being present in the oxidation state + 2.[41,60] The detailed spectrum for the Fe 2p emission line exhibits a peak at a binding energy of 710.6 eV corresponding to the Fe $2p_{3/2}$ energy level, while the peak at 724.6 eV can be ascribed to Fe $2p_{1/2}$. Especially the presence of the satellites between 721 eV and 716 eV, and 736 eV and 730 eV, respectively, suggest the presence of iron species as both Fe^{2+} and Fe^{3+}.[60,61] The O 1s photoemission (Figure S4C) at the binding energy of 530.0 eV corresponds to metal-oxide bonds.[60] Furthermore, the O 1s high-resolution spectra (Figure S4C) show for all CFOs the presence of a shoulder between 533 eV and 531 eV, which is indicative of defective oxygen.[62,63] Since the shapes of the shoulders are the same for all CFOs, the defective oxygen (including oxygen vacancies) can be considered equal in terms of their concentrations. For all samples no reduced species, such as Cu^+ or Cu^0, were detected. Apart from a weak C 1s peak at 284.9 eV,[64] which is attributed to adventitious (surface-adsorbed) hydrocarbons rather than from

Chem. Eur. J. **2023**, *29*, e202300277 (4 of 16)

© 2023 The Authors. Chemistry - A European Journal published by Wiley-VCH GmbH

Chemistry–A European Journal

Research Article
doi.org/10.1002/chem.202300277

Chemistry Europe
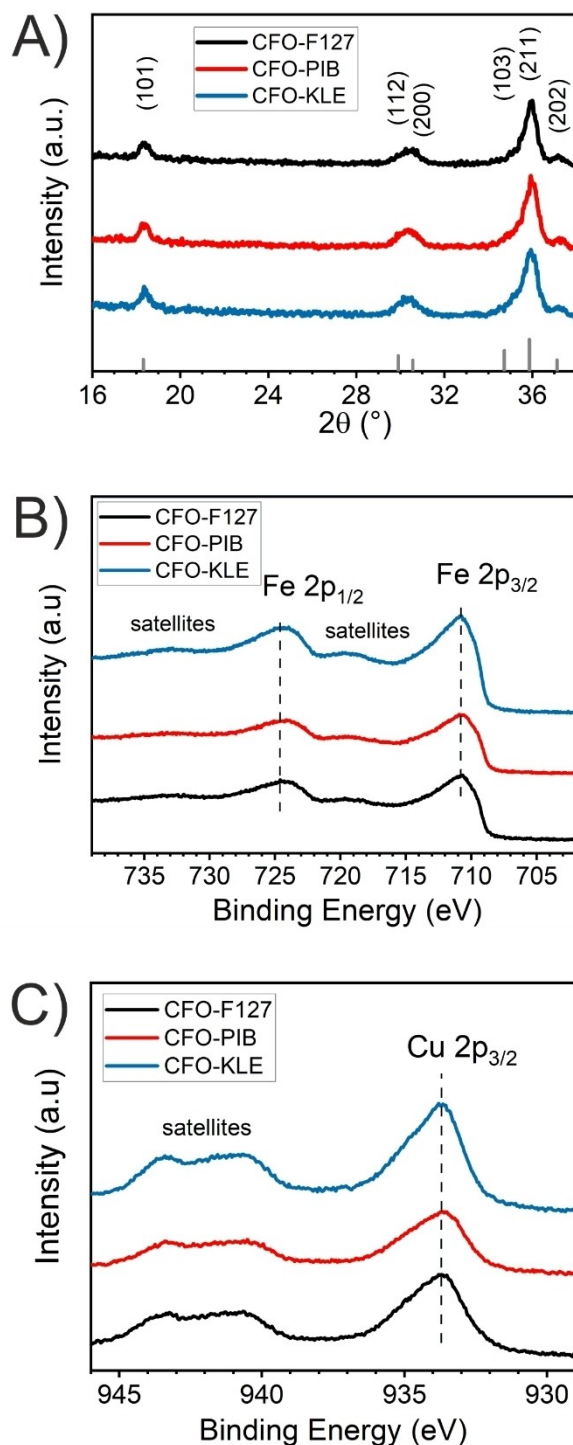European Chemical
Societies Publishing

Figure 2. Structural characterization of the CFO-F127 (black), CFO-PIB (red), and CFO-KLE (blue) samples: A) GIXRD patterns with reference bars (gray) according to JCPDS no. 034–0425 (space group I 4_1/a m d) for the tetragonal spinel phase, B) detailed photoemission spectra of Fe 2p and C) Cu 2p determined by XPS.

residual organic template due to the high calcination temperature, low concentrations of Na were detected (Figure S4A). The impurities, most likely originating from the synthesis, were found to be approximately 1% for all samples and can therefore be taken as comparable in content considering an experimental error of ±5%. It is noteworthy that the Na 1s signals were not observed after cleaning/rinsing the CFO samples with deionized water prior to XPS analysis, which implies that the contami-

Chemistry–A European Journal

Research Article
doi.org/10.1002/chem.202300277

Chemistry Europe
European Chemical
Societies Publishing

nation is present as surface adsorbed species. The chemical surface composition was determined to be $Cu_{0.97}Fe_{1.64}O_{4.33}$, $Cu_{0.8}Fe_{1.41}O_{4.75}$, and $Cu_{0.91}Fe_{1.9}O_{4.01}$ for the CFO-F127, CFO-PIB, and CFO-KLE, respectively. The data imply that crystal structure formation of the spinel phase is most accurate in terms of elemental composition for the KLE-based CFO. The deviation from the ideal stoichiometry (M_3O_4) can be explained by the fact that XPS analysis provides only information of the first few atomic layers (representing the surface) and can therefore be considered *per se* as a defective structure (broken crystal structure symmetries, dangling bonds etc.).

Optoelectronic characterization

The optical absorption properties of the CFO-F-127, CFO-PIB, and CFO-KLE thin films were evaluated by UV-vis spectroscopy (Figure 3). In Figure 3A, the absorbance spectra of all samples between a wavelength range of 280–1000 nm are shown, revealing a strong absorption in the visible range between 300 nm and 600 nm. It is noteworthy that the CFO-F127 films possess the strongest absorption (followed by the CFO-PIB), especially for wavelengths below 500 nm. This trend can be ascribed to the slightly increased film thickness of the CFO-F127 samples, which was determined to be (190 ± 15) nm by profilometry (see Figure S5), compared to CFO-PIB (180 ± 15) nm and CFO-KLE (170 ± 15) nm. The observed film thicknesses are reasonable and in agreement with other structurally related mesoporous metal oxides prepared by soft-templating.[53,62,65] In consequence, the absorption coefficients are comparable among the three CFO samples allowing interpretation of the photoelectrochemical properties according to similar light absorption/photoexcitation. In principle, the absorbance of photons can be attributed to both direct (non-phonon assisted) and indirect (phonon-assisted) optical transition processes within the $CuFe_2O_4$ thin films.[66] The direct ($m = 2$) and indirect ($m = 1/2$) optical band gap can be determined by using an energy dependence relation of $\alpha h\nu = (h\nu - E_g)^m$, where α and E_g are the absorption coefficient and the energy gap of the semiconductor, respectively. To determine the band
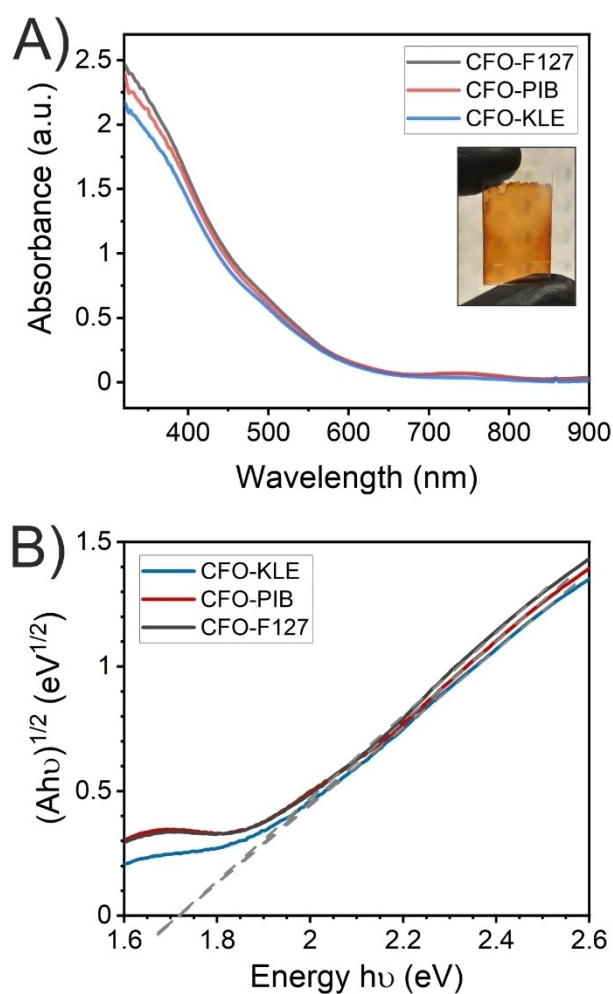

Figure 3. A) Absorbance spectra and B) Tauc plots for an indirect optical transition of the mesoporous CFO-F127 (black), CFO-PIB (red), and CFO-KLE (blue) samples. The gray dotted lines serve as guidance for the eyes for graphical estimation of the band gap energies.

Chemistry–A European Journal

Research Article
doi.org/10.1002/chem.202300277

Chemistry
Europe
European Chemical
Societies Publishing

gap from the Tauc plots (Figure 3B), $(Ah\nu)^m$, where A is the absorbance and $h\nu$ is photon energy, was plotted against the photon energy. The intercept with the x-axis in the Tauc plot provides the optical band gaps of the CFO samples, which were found to be (1.7 ± 0.05) eV for all indirect optical transitions. The direct optical band gap energies were also calculated (Figure S6) and determined to be (2.3 ± 0.05) eV for all CFO thin films. The obtained values for both indirect and direct band gaps are in good agreement with other $CuFe_2O_4$ photoelectrodes.[10]

The secondary electron cut-off (work function) and the valence band maxima (VBM) were determined through detailed XPS analysis (Figure S4C) and are discussed together with the data from UV-vis spectroscopy. Considering the obtained band gap energies (note that CFO is mainly described as indirect semiconductor in literature), work functions and VBM, the energy band diagrams for the CFO-F127, CFO-PIB, and CFO-KLE thin films were determined (Figure 4). As illustrated in Figure S4C, for all samples, the Fermi energy was evaluated to be 1.3 eV above the VBM, whereas the work function was found to be (4.5 ± 0.1) eV, (4.8 ± 0.1) eV, and (4.7 ± 0.1) eV for the CFO-KLE, CFO-PIB, and CFO-F127, respectively.

Therefore, the energetic position of the conduction band (CB) was the highest for the CFO-KLE and lowest for the CFO-F127 (Figure 4). Conclusively, all mesoporous CFO thin films are theoretically capable of performing overall solar water splitting owing to the fact that the CB straddles the reduction potential (0 eV vs. NHE) and the VB (1.23 eV vs. RHE) the oxidation potential of water.

Photoelectrochemistry

Before investigating the CFO thin films under illuminated conditions and applied as photoelectrodes for photoelectrochemical water splitting, the redox reactions occurring in alkaline media under non-irradiated (dark) conditions were elucidated by cyclic voltammetry (CV). Figure 5A exhibits the CV curves of the CFO-KLE, CFO-PIB, and CFO-F127 thin films

including the oxidation and reduction processes of the iron and copper species in alkaline media (0.1 M NaOH, pH 12.8). For all samples oxidation peaks referred to Fe^{2+} to Fe^{3+} (at 0.4 V vs. RHE) and Cu^{+1} to Cu^{2+} (at 0.9 V vs. RHE) appear when scanning the potentials from 0 V to 1.6 V vs. RHE. For the backward scans, three reduction processes can be considered as Cu^{2+} to Cu^{1+} (less pronounced peaks at 0.9 V vs. RHE), Cu^{1+} to Cu^0 (at 0.4 V vs. RHE), and Fe^{3+} to Fe^{2+} (at 0 V vs. RHE). Considering the Pourbaix diagram for iron,[67] the reduction of iron (III) to iron (II) is likely, which is close to 0 V vs. RHE. We note that the reduction of copper ions occurs electrochemically in the range of cathodic sweeps and that the reductive species are reported to be soluble in alkaline media.[68] These findings explain the instability of CFO photocathodes for cathodic potentials already in the absence of light (dark), which was additionally proven through 20 consecutive CV scans at 50 mV/s (Figure S7). The data show that the corresponding reduction and oxidation peaks become less prominent in following cycles, indicating dissolution of films. Interestingly, the copper reduction peak is less pronounced for the CFO-KLE sample, which might be interpreted as that ordered mesoporous CFO are more stable in alkaline media. Since the underlying mesoporous CFO thin films are found to be n-type semiconductors (and thus applied as photoanodes), the photoelectrochemical experiments were only performed between 0.8 V to 1.6 V vs. RHE (as described below). Consequently, the reduction of Cu^{2+} to Cu^{1+} and its back-oxidation can be considered as the only relevant redox reactions (considering electrochemical changes of the CFO materials).

The mesoporous CFO thin films were photoelectrochemically characterized as photoabsorbers for solar water splitting. Figures 5B and C display the intermittent light voltammetry plots (light period times of 10 s) which have been measured with a white light LED having an intensity of 100 mW/cm² and between a potential window of 0.8–1.6 V vs. RHE. All samples show anodic (photo−) currents as expected for liquid junction with an n-type semiconductor. Both p-type and n-type characteristics have been reported for CFO photoelectrodes in literature.[10] When comparing the three CFO thin films for the
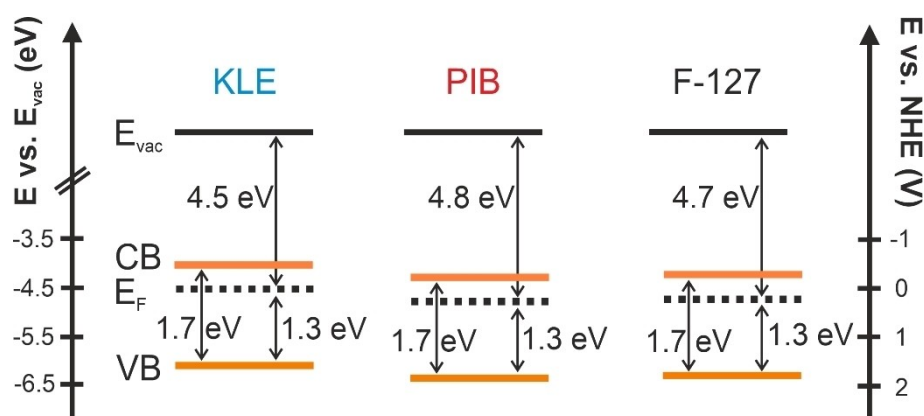

Figure 4. Energy band diagrams of the mesoporous CFO-F127 (black), CFO-PIB (red), and CFO-KLE (blue) samples. The energy diagrams were derived by evaluation of XPS and UV-vis spectroscopy and visualize the energetic positions of the valence band (VB), conduction band (CB), and Fermi energy (E_F) with respect to both E_{vac} and E_{NHE}.
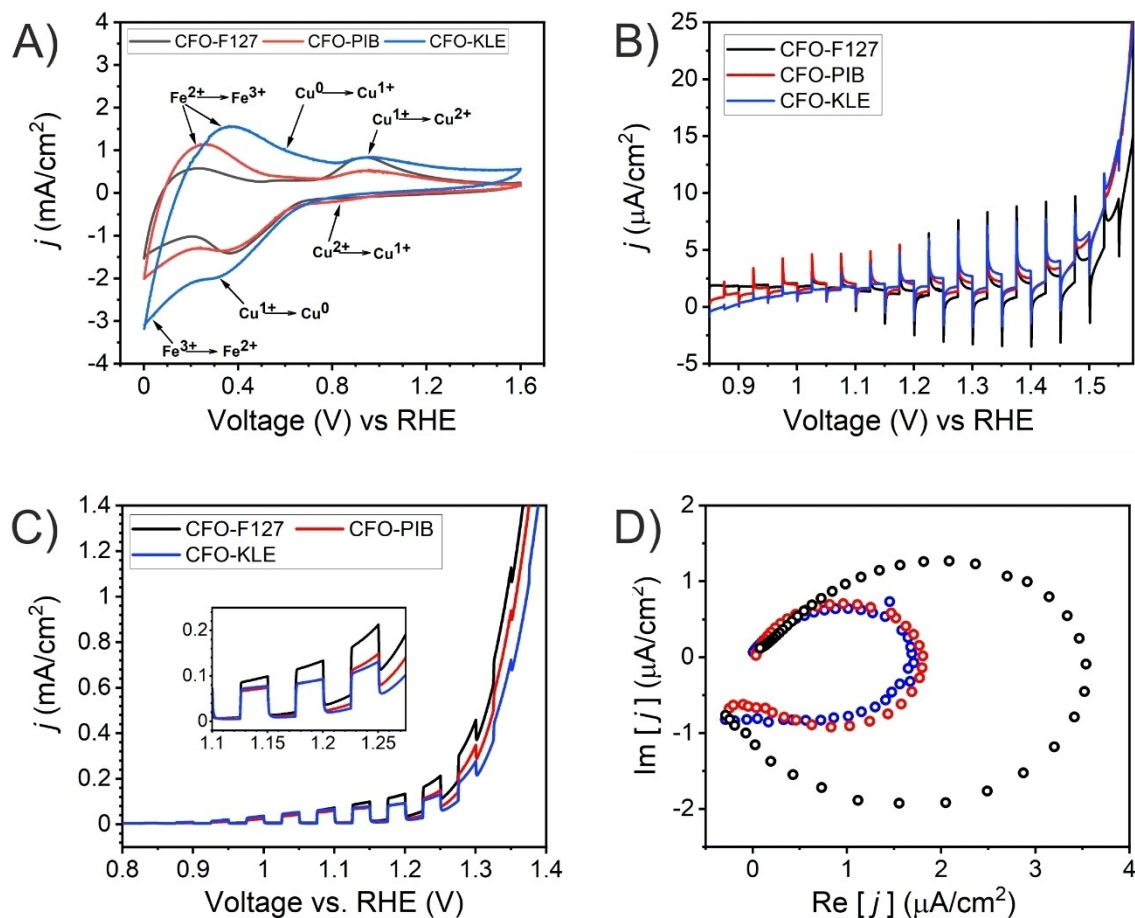
Chemistry–A European Journal

Research Article
doi.org/10.1002/chem.202300277

Chemistry Europe
European Chemical
Societies Publishing

Figure 5. A) Comparison of cyclic voltammetry scans in 0.1 M NaOH, intermittent-light voltammetry in B) 1 M NaOH and C) 0.1 M NaOH and 1 M Na_2SO_3 (hole scavenger), and D) intensity modulated photocurrent spectroscopy of the mesoporous CFO-F127 (black), CFO-PIB (red), and CFO-KLE (blue). All experiments were carried out in a 3-electrode setup utilizing Hg/HgO as reference electrode (pH 12.9).

water oxidation reaction analyzed in 0.1 M NaOH solution (pH 12.9), the highly ordered CFO-KLE photoanodes showed the highest steady-state photocurrent density (reached and settled in after a couple of seconds) of 2.7 $\mu A/cm^2$ at 1.23 eV vs. RHE, followed by the CFO-PIB with 2.0 $\mu A/cm^2$, and CFO-F127 (1.5 $\mu A/cm^2$). Interestingly, when comparing the same CFO samples with respect to sulfite oxidation (Figure 5C), the opposite trend in photoactivity was attained, showing the highest photocurrent density for the disordered CFO-F127, which amounted to 0.18 mA/cm^2 and 0.46 mA/cm^2 at 1.23 V and 1.3 V vs. RHE, respectively. The ordered CFO-PIB and CFO-KLE possessed photocurrent densities of 0.125 mA/cm^2 and 0.115 mA/cm^2 at 1.23 V vs. RHE, respectively. Photocurrent transients are suppressed due to the fact that one-hole sulfite oxidation is much faster than four-hole water oxidation. Water oxidation requires accumulation of three or more holes at the surface.[69] This is accompanied by surface electron-hole recombination and causes the transient photocurrent response in Figure 5B.[70,71] The observed increase of transients in order CFO-KLE < CFO-PIB < CFO-F127 suggests that the pore ordering indeed has an impact on these (surface) recombination

processes. To better understand and interpret the (contrary) photoactivity trends, IMPS investigations were carried out to provide information about the bulk charge carrier dynamics and recombination processes occurring at the surface of the mesoporous CFO films. During IMPS, the phase shift of the photocurrent when applying a sinusoidal perturbation of the light source is measured.[72,73] In this form of impedance spectroscopy-based analysis, it is assumed that the minor changes in light intensity solely alter the concentration in surface charge carriers, while the band bending remains unaffected.[74] In general, IMPS allows probing how the (real part) of photocurrent of a PEC system responds to the light perturbation input. When plotting the complex photocurrent in dependence of the light perturbation frequency, the charge transfer rate (k_{trans}) and the surface recombination rate (k_{rec}) can be extracted from the corresponding semicircle plots. Here, the semicircle is composed of a high- (HFI, in the second quadrant) and low-frequency intersect (LFI, in the first quadrant) with the real axis. As reported in literature, the HFI directly correlates to the flux of charge carriers (here holes) moving toward the photoelectrode surface (which corresponds to the semiconduc-

Chemistry–A European Journal

Research Article
doi.org/10.1002/chem.202300277

**Chemistry
Europe**
European Chemical
Societies Publishing

tor/liquid junction, SCLJ), while LFI represents the steady-state photocurrent, which provides the rate transferring the charges to the electrolyte for water oxidation.[75,76] From the ratio between LFI and HFI, the charge transfer efficiency (η_{CT}) can be derived which is defined as $k_{trans}/(k_{trans} + k_{rec})$. The mechanisms of IMPS have been extensively studied by Peter et al.[72,77] and are well studied for α-Fe$_2$O$_3$[76] and CuFe$_2$O$_4$[26] photoelectrodes. In agreement with the photocurrent transients derived by intermittent light voltammetry experiments, the most ordered mesoporous CFO-KLE showed the lowest surface recombination rate with $k_{rec} = 123$ s^{-1} followed by the slightly ordered CFO-PIB system with 155 s^{-1}. The highest surface recombination rate was obtained for the non-ordered CFO-F127 materials (192 s^{-1}). At the same time, the CFO-F127 illustrated the highest charge carrier transfer rate of $k_{trans} = 9.3$ s^{-1} compared to CFO-PIB (2.9 s^{-1}) and CFO-KLE thin films (2.5 s^{-1}). Evaluation of the data result in a charge carrier transfer efficiency of about 5% for F-127 templated samples, which is 2.5 times higher compared to 2% for the ordered mesoporous CFO systems. The data help to explain the PEC response of mesoporous CFO materials and demonstrate that non-ordered CFO thin films possess the highest over-shoot photocurrent due to fast bulk charge carrier transfer most likely owing to high crystallinity affecting the electronic structure and thus charge carrier transport. Also, the results clearly indicate that for CFO-F127 a greater portion of photo-initiated charge carriers reach the surface of the material (highest k_{trans}), but severe surface recombination (highest k_{rec}) seems to impede charge carrier transfer to the aqueous electrolyte for the subsequent water oxidation reaction (and thus oxygen evolution), which can be in turn predominantly assigned to the largest surface area of CFO-F127 (see determination of double-layer capacitance). These findings are reasonable, since the water oxidation is known to be a kinetically slow reaction and thermodynamically uphill process, and is therefore mainly limited by the surface recombination rate.[69,78] In contrast, the sulfite oxidation is a fast reaction and additionally

thermodynamically favorable (compare oxidation potentials of water and sulfite in Figure 6) and is therefore controlled by the surface area. In conclusion, it can be stated that high-surface-area photoelectrodes can be generally considered as suitable for driving thermodynamically favorable processes (controlled by surface area), while lower surface area photoabsorbers seems to be beneficial for driving thermodynamically uphill processes.[78]

Furthermore, all mesoporous CFO thin films – regardless of the template – show in general very high absolute surface recombination rates when compared to other solution-processed CFO thin films, typically possessing values between 2 and 8 s^{-1} (for pH 13.6 and between 1.6 V and 0.7 V vs. RHE).[26] This comparison reveals that mesoporous materials suffer under severe surface recombination owing to their large surface areas, offering at the same time plenty of reaction sites and surface defects (mid-gap states), which act as recombination centers for migrating charge carriers. When comparing the photoresponse of the CFO-F127 with mesoporous ZnFe$_2$O$_4$ photoanodes (also prepared with Pluronic® F-127 as porogen and under the same synthetic conditions),[21] a three times enhanced PEC performance was found. Therefore, the photoresponse of mesoporous CFO thin films (in the presence of a hole scavenger) can be considered as one of the highest values reported for sol-gel derived (n-type) CFOs and shows the best PEC performance among any mesoporous ferrite photoanode.

To further assess photochemical charge separation of the CFO-liquid interface, vibrating Kelvin probe surface photovoltage spectroscopy (VKP-SPS) was used. VKP-SPS measures the contact potential difference (CPD) of thin film structures under excitation with light.[78–84] The resulting CPD change equals the surface photovoltage signal SPV = CPD(light) − CPD(dark). The advantage of SPS compared to conventional photoelectrochemical characterization techniques is the high sensitivity of the method, since already small charge carrier concentrations (10^{10} per cm^{-2}) result in potentials on the mV
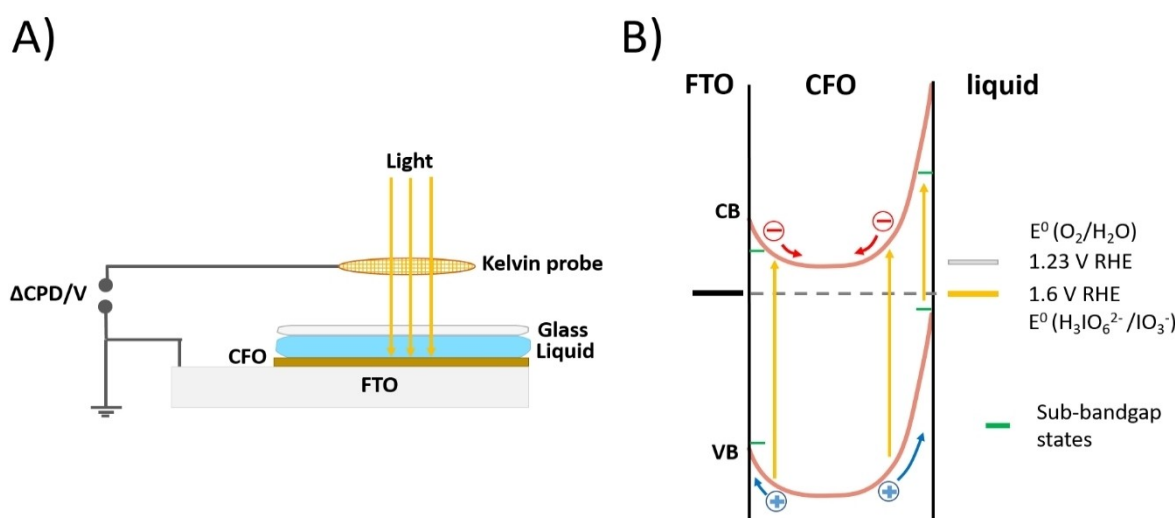

Figure 6. A) Measurement configuration for liquid SPS. B) Charge transfer scheme for SPS showing depletion of CFO at the front and back contacts and charge transfer under bandgap and sub-band gap excitation. E^0(NaIO$_4$/NaIO$_3$) = 1.60 V vs. RHE.[87]

Chemistry–A European Journal

Research Article
doi.org/10.1002/chem.202300277

Chemistry Europe
European Chemical
Societies Publishing

scale.[85] Recently, we have expanded VKP-SPS to include solid-liquid interfaces.[86] This is possible by covering the sample with a drop of the electrolyte and a glass cover slip, as shown in Figure 6A. In order to achieve an anodic bias as in Figure 5, 0.02 M aqueous $NaIO_4$ as electrolyte was employed. This oxidizing reagent ensures depletion of the CFO as shown in Figure 6B.

SPV spectra recorded under these conditions are shown in Figure 7A. All samples produce a negative photovoltage at photon energies above 1.4 eV and a small positive (inverted) photovoltage signal at 1.2–1.6 eV. The larger, negative signal is attributed to hole transfer to the CFO-liquid interface. This signal is created by band gap excitation of the material and corresponds to the transfer of photogenerated holes to the CFO-liquid interface. This is analogous to the anodic behavior of CFO as seen in the electrochemical scans under applied bias. The 1.4 eV onset for the negative photovoltage is about 0.3 eV below the optical band gap of the material. We attribute this shift to excitation of band-tail states (as shown in Figure 6A) near the CFO interfaces. Additionally, a Franz-Kheldysh effect (the narrowing of the band gap by an electric field) is likely responsible.[88–91] The electric field is maximum at the CFO-interface. It is the direct result of the depletion of CFO by the $NaIO_4$ reagent. The shape of the inverted photovoltage signal at 1.2–1.6 eV and of the negative photovoltage branch is caused by the emission spectrum of the Xe lamp/monochromator configuration (see Figure S3 in [92]). Maximum SPV values are observed near 3.0 eV and increase in the order CFO-F127 (20 mV) < CFO-PIB-PEO (48 mV) < CFO-KLE (52 mV). This is in good agreement with the IMPS results which suggest that surface recombination (the reason for the photovoltage loss) is lowest for the PIB- and KLE-based ordered mesoporous CFOs. The results of both characterization techniques taken together support the conclusion of a lower surface defect concentration for the ordered mesoporous systems. Lastly, the small positive photovoltage at 1.2–1.6 V in all samples is assigned to carrier transfer near the CFO-FTO contact. Based on the work function data in Figure 4, a Schottky junction is expected here, as shown in Figure 6B. This junction attracts photogenerated holes (minority carriers) to the FTO, which is opposite of the desired charge transfer direction during photoelectrochemical water oxidation. This is the cause for the positive SPV signal. The photovoltage is seen at low photon energy, where the light penetration depth of CFO is largest, so that the photons can excite the back of the film. We have previously observed a similar behavior in $SrTiO_3$ and GaAs films on gold.[93] On this basis, the Schottky junction at the FTO-CFO contact is a contributor to the photovoltage loss and the low photocurrent in the PEC data.

In order to determine the flat band potential, which is an important characteristic to evaluate the photoonset potential of a photoelectrode, Mott-Schottky analyses were conducted for all CFO samples in dark (without illumination). From the trend of the plots presented in Figure 7B, n-type conductivity is evident since all three samples possess positive slopes for the $1/C^2$-voltage dependence. Moreover, the flat band potentials were determined from the slope (according to equation E1 in
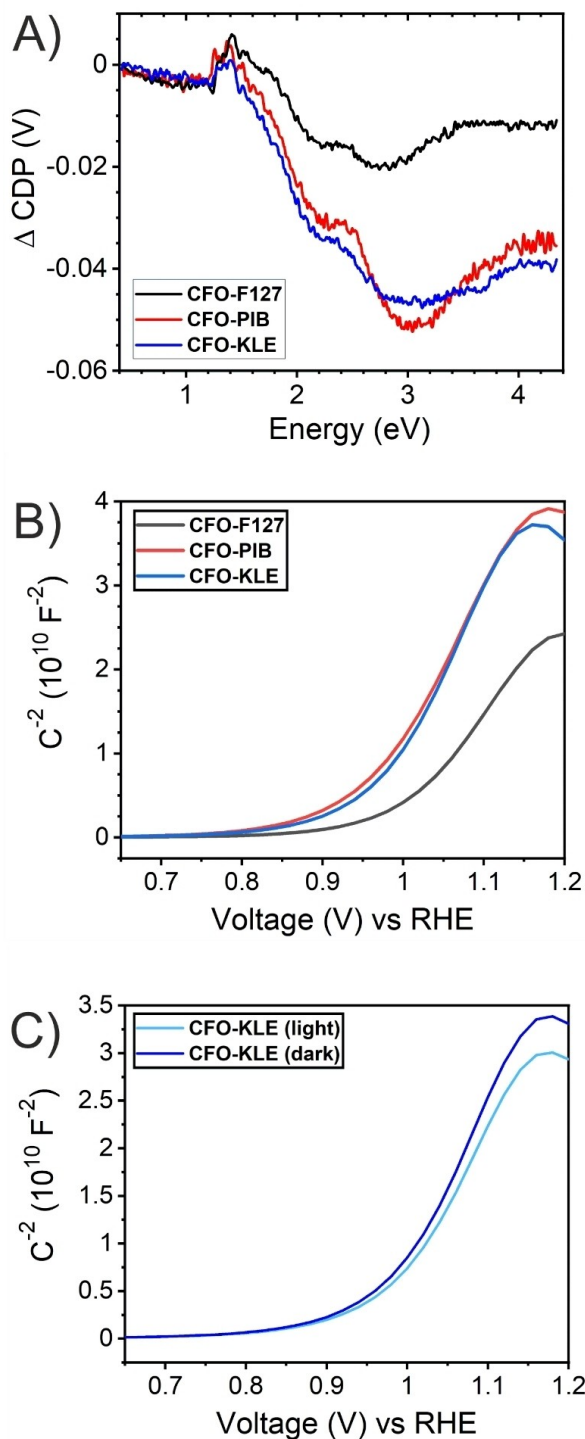

Figure 7. A) Surface photovoltage spectra acquired for CFO immersed in aqueous 0.2 M $NaIO_4$ solution. B) Mott-Schottky analysis of the CFO-F127, CFO-PIB, and CFO-KLE thin film photoelectrodes analysed in the dark. C) Mott-Schottky analysis of the CFO-KLE in dark and under illumination (white light LED 100 mW/cm²). These experiments were conducted in 0.1 M NaOH (pH 12.9).

the Supporting Information), showing a value of about 0.95 V vs. RHE for CFO-PIB and CFO-KLE and 0.98 V vs. RHE for the

Chem. Eur. J. **2023**, *29*, e202300277 (10 of 16)

© 2023 The Authors. Chemistry - A European Journal published by Wiley-VCH GmbH

Chemistry–A European Journal

Research Article
doi.org/10.1002/chem.202300277

Chemistry Europe
European Chemical
Societies Publishing

CFO-F127-based photoanodes. These values are in agreement with the photo-onset potentials derived from Figure 5B showing the first photoresponse at (0.875 ± 0.025) V vs. RHE for all samples. The observed flat band potentials were slightly higher than the ones reported for solution-based chemical bath deposition (CBD) derived CFO thin films (0.78 V vs. RHE)[26] and in agreement with other CFO nanostructures (0.85–0.90 V vs. RHE) prepared by a wet-chemical approach and treated at 750°C.[27] When comparing the flatband potentials of CFO-KLE measured in dark and under illumination (Figure 7C), an interesting feature becomes apparent, which is the shift of the V_{FB} from 0.98 to 0.94 V vs. RHE. This positive shift of V_{FB} is associated to the population of surface states by charge carriers resulting in downward shift of the band edges.[26,94] All experimentally obtained materials parameters of the CFO samples are summarized for sake of comparison in Table 1. Uniform and homogenous thin films possessing an ordered mesoporous network are generally suitable model systems for monitoring structural and morphological changes at the surface during or after (catalytic) applications by micro- and/or spectroscopic tools. Therefore, the CFO-KLE samples, possessing a defined surface structure, were chosen as control sample in order to elucidate whether the ordered mesoporous CFO framework was structurally affected or changed by the PEC experiments. Figure 8 shows SEM images of the CFO-KLE thin films (on FTO substrates) before (Figure 8A) and after (Figure 8B) performing chronopotentiometry experiments at 1.23 V vs. RHE in 0.1 M NaOH for 1 h under illumination with a white-light LED (100 mW/cm²). Interestingly, the SEM investigations reveal that the illuminated and electrolyte-exposed area of the CFO-KLE photoelectrode remains structurally intact in terms of preservation of the ordered mesoporous architecture after PEC operation. Consequently, it can be concluded that neither the contact with the aqueous electrolyte nor the illumination upon PEC operation significantly affect the mesopore arrangement of CFO-KLE photoanodes. These results are further supported by XPS data as depicted in Figures 8C and S8A and B. XPS spectra were recorded for the CFO-KLE after the same PEC analysis as

described above and were compared with the as-prepared samples. No changes in binding energies and photoemission peak shapes were found as presented for the Fe 2p (Figure S8A) and Cu 2p signals (Figure S8B). However, the O 1s spectrum exhibits beside the main peak at 530 eV (referred to metal-oxygen bonds)[95] a decrease of the shoulder located at binding energies between 531 eV and 533 eV. This feature is generally ascribed to defective and low-coordinated oxygen configurations, such as oxygen vacancies, surface-adsorbed oxygen/hydroxyl groups, and surface adsorbed water.[63] Since it was reported for defective hematite surfaces that OH fills the oxygen vacancy position during dissociative water adsorption,[96,97] the defective oxygen groups, which appear to be less prominent in the O 1s spectra of CFO-KLE after PEC investigations (Figure 7C), therefore might be interpreted as a photoinduced healing process of these surface oxygen vacancies or as removal of C—O species from adventitious carbon.

Optimization of PEC performance

Since not only the calcination temperature, but also the holding time has been demonstrated to have major impact on the photoelectrochemical properties of metal oxide-based photoelectrodes due to extensive increase of crystallinity,[15,21] the mesoporous CFO thin films were also photoelectrochemically characterized after prolonged annealing time. All synthetic parameters were kept otherwise constant except for the calcination holding time, which was changed from 10 min to 12 h at 600°C. Because any change in surface morphology upon/after sintering at this elevated temperature can be ideally detected on well-ordered surface morphologies, again, we chose the ordered mesoporous CFO-KLE samples as control sample. Figure 9A shows the SEM image of the CFO-KLE thin film calcined for 12 h. The images show that the increase in holding time changed the pore morphology significantly due to sintering of nanocrystals within the pore walls, resulting in a breakdown of the ordered mesoporous framework. Interestingly, even after 12 h calcination, separated mesopores with well-developed cylindrical shapes were sporadically still present. The GI-XRD pattern (Figure S9) demonstrates more pronounced and intense peaks compared to the Bragg signals observed in the diffractograms for the 10 min calcined CFOs. All peaks can be indexed according to the tetragonal spinel phase (JCPDS 034-0425). The 12 h calcined CFO-KLE samples possess drastically enhanced photocurrent densities of 0.37 mA/cm² compared to the 0.18 mA/cm² of the 10 min calcined CFO counterpart by almost doubling the photocurrent density when measured at 1.3 V vs. RHE in 0.1 M NaOH containing 1 M Na_2SO_3. Since the absorption of light was not enhanced for the 12 h (Figure S10) compared to 10 min calcined CFO-KLE samples (Figure 3), the improved PEC response is most likely attributed to the increase of crystallinity and the development of larger CFO domains possessing less defect sites.

The rise in crystallinity is typically linked to enhanced electronic transport properties due to a decline of defective sites leading to increased mean free paths of the (photo-

Table 1. Tabular summary of the structural and (photo-) electrochemical parameters obtained from the experiments conducted on F-127, PIB, and KLE templated mesoporous CFO thin films calcined for 10 min at 600°C in air.

Properties/Material	CFO-KLE	CFO-PIB	CFO-F-127
Pore diameter [nm]	15-20	16-22	12-18
Crystallite size [nm]	14	14	14
Direct/indirect band gap [eV]	2.3/1.7	2.3/1.7	2.3/1.7
Work function [eV]	4.5	4.8	4.7
Photocurrent density at 1.23 V vs. RHE in 0.1 M NaOH [$\mu A\,cm^{-2}$]	2.7	2.0	1.5
Photocurrent density at 1.23 V vs. RHE in 0.1 M NaOH and 1 M Na_2SO_3 [$\mu A\,cm^{-2}$]	115	125	180
Bulk transfer rate [s^{-1}]	2.5	2.9	9.3
Surface recombination rate [s^{-1}]	123	155	192
Flat band potential vs. RHE [V]	0.9	0.9	0.9
Double-layer capacitance [mF]	0.107	0.097	0.195
Surface photovoltage [mV]	48	52	20

Chemistry–A European Journal

Research Article
doi.org/10.1002/chem.202300277

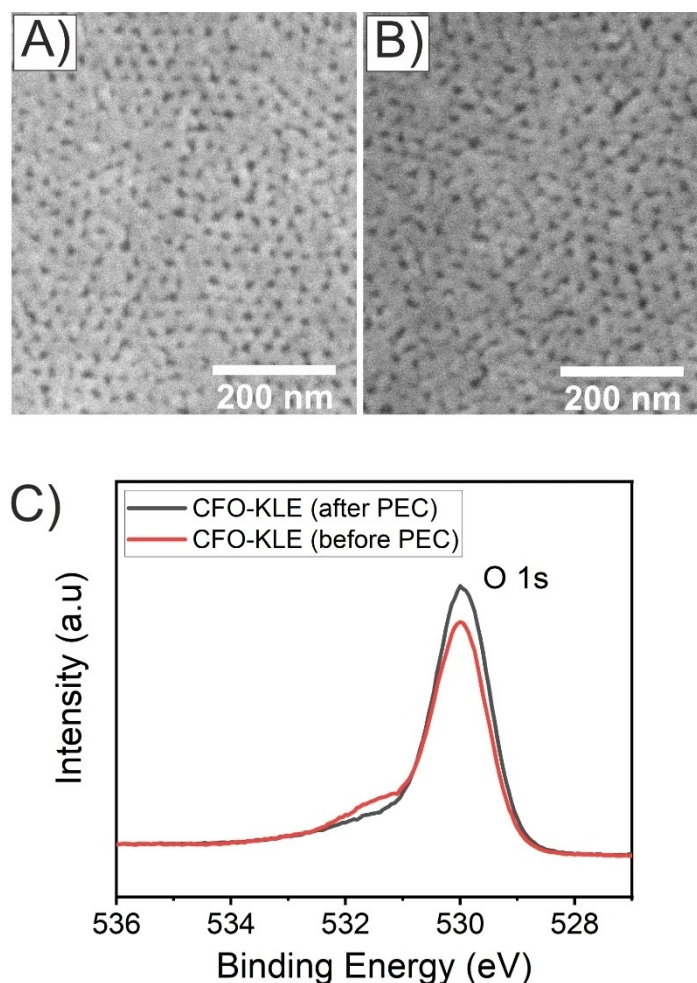**Chemistry Europe**
European Chemical
Societies Publishing

Figure 8. Post-PEC characterization of the mesoporous CFO-KLE samples: SEM images in high magnification A) before and B) after PEC measurements, and C) fine scan O 1s spectra determined by XPS before (red lines) and after PEC (black lines).

initiated) charge carriers. This explanation is in good accordance with the observed photoactivity dependence of CuO nanofibers on their annealing time.[15] The 12 h calcined CFO films were further compared in terms of comparing distinct excitations sources. Therefore, the CFO materials were investigated through a white-light LED (100 mW/cm^2, $\lambda_{max} = 562$ nm) and a UV-light LED (100 mW/cm^2, $\lambda_{max} = 369$ nm) both possessing the same illumination intensity (corresponding to the solar spectral irradiance AM 1.5e G). The CFO-KLE films irradiated with UV-light exhibit photocurrent densities of 0.3 mA/cm^2 and 0.5 mA/cm^2 at 1.23 V and 1.3 V vs. RHE, respectively, which was found to be as a substantial increase of 35 % when compared to the PEC performance of CFO samples illuminated with a white-light LED (Figure 7C). The significant difference in PEC performance can be ascribed to the absorption of high-frequency photons from the UV-source, which will be absorbed by the CFO-KLE samples to a much larger extent compared to low-energy photons. At an excitation wavelength of 369 nm, every photon possesses enough and even more energy (369 nm corresponds to 3.36 eV) to excite an electron-hole pair above the band edges of the CFO-KLE (band gap energies were found to be

1.6 eV and 2.3 eV for direct and indirect transitions, respectively, compare Figure 3B and S6). In essence, electrons and holes can also be photoexcited to supra-conduction and sub-valence band states (energetically much higher than near-band-edge states), respectively. These hot charge carriers are known to relax to near-band-edge states or directly react with the specific redox species (from the electrolyte), explaining the enhanced photoresponse observed for UV-irradiated CFO samples.[98,99] In this context, Polo et al. recently demonstrated that the PEC water splitting performance of sol-gel derived ZnFe$_2$O$_4$ thin films can be effectively enhanced by tailoring key parameters such as the calcination procedure and film thickness.[100] Therefore, the underlying results on CFO photoanodes might be transferred to other metal oxide photoabsorber materials for further improvement of their PEC properties through tailoring of synthesis parameters.
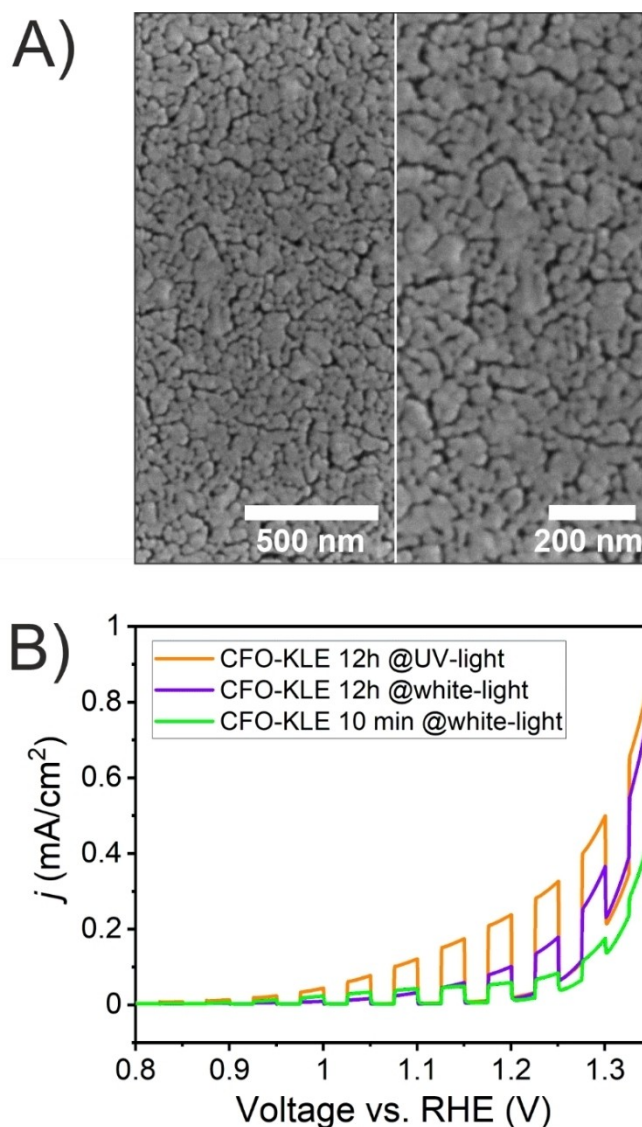
Chemistry–A European Journal

Research Article
doi.org/10.1002/chem.202300277

Chemistry Europe
European Chemical
Societies Publishing

Figure 9. Characterisation of the CFO-KLE thin films treated at 600 °C for 12 h: A) SEM images in low (left) and high magnification (right), and C) intermittent-light voltammetry operated with UV-light LED ($\lambda = 365$ nm, orange line), a white-light LED (violet line). The performance of the 10 min calcined CFO-KLE illuminated with a white light LED is shown for comparison (green line). All experiments were conducted in 0.1 M NaOH and 1 M Na_2SO_3 (pH 12.9).

Conclusion

Mesoporous CFO thin films with different degree of pore ordering and surface morphologies were prepared by soft-templating in order to study the impact of structural features on the PEC properties. The change of surface morphology was chosen as control parameter and was realized by utilizing Pluronic® F-127, PIB-PEO, and KLE as structure directing agents. In this way non-ordered, slightly ordered and ordered CFO photoanodes could be synthesized and systematically compared to each other in terms of morphology, crystallographic structure and their (photo-) electrochemical properties. The energy band diagrams of the CFOs derived by XPS analysis illustrate that all photoabsorbers are theoretically capable of performing overall solar water splitting with respect to their energetic band alignments. When characterizing the CFOs photoelectrochemically, an opposite trend regarding sulfite and water oxidation was found: while the non-ordered CFO thin films possessed the best PEC performance for sulfite oxidation, the most ordered KLE-templated CFO demonstrated the highest (80 % increased) photoresponse for photoelectrochemical water oxidation. Since sulfite oxidation is a thermodynamically favorable (fast) reaction, it is controlled by the surface area of the mesoporous CFO thin films. This is why the highest surface area was found for the Pluronic® F-127-based CFO. In contrast, the much slower water oxidation is thermodynamically uphill and limited by surface recombination. This was confirmed by both VKP-SPS and IMPS data, revealing that the KLE-templated ordered mesoporous CFO thin films possess the lowest amount of surface defects corresponding to the highest surface photo-voltage. The Schottky junction at the FTO-CFO interface, which traps electrons, was found to be partially responsible for the

Chemistry–A European Journal

Research Article
doi.org/10.1002/chem.202300277

Chemistry Europe
European Chemical
Societies Publishing

low observed photocurrent and -voltage of the CFO electrodes. Conclusively, this work exemplifies the principle that high-surface-area photoelectrodes are preferred for driving thermodynamically favorable reactions (sulfite oxidation), while lower surface area photoelectrodes are beneficial for driving thermodynamically uphill processes (water oxidation). Based on this knowledge, novel synthetic optimization attempts might be realised by combining highly crystalline structures with less defective surface morphologies for the fabrication of high-performance CFO-based PEC devices.

Experimental Section

Materials: The chemicals that have been used for the preparation of mesoporous $CuFe_2O_4$ thin films are iron (III) nitrate nonahydrate (Fe $(NO_3)_3 \cdot 9\ H_2O$, $>99.9\%$, Sigma Aldrich), copper (II) nitrate trihydrate $(Cu(NO_3)_2 \cdot 3\ H_2O$, $>99\%$, Sigma Aldrich), 2-methoxyethanol (99.8%, Sigma Aldrich), ethanol (99%, Sigma Aldrich), Pluronic® F-127 (Sigma Aldrich), PIB-PEO synthesized as described in[52]) and KLE (synthesized as described earlier[40]). Silicon (100) wafers (Siltronic), fluorine doped tin oxide (FTO) coated Pilkington TEC glass slides (Xop Glass) was used as a substrate.

Preparation of CFO Thin Films: The stoichiometric composition of dip-coating solution were prepared by adding 0.335 g of Fe $(NO_3)_3 \cdot 9H_2O$, 0.101 g Cu $(NO_3)_2 \cdot 3H_2O$ in 1.6 mL of ethanol, while 45 mg of structure-directing agents (Pluronic® F-127, PIB, or KLE) were dissolved in 0.6 mL of 2-methoxyethanol. Both solutions were stirred/shaked for 30 min until a homogeneous solution was obtained. Afterwards both solutions were combined, followed by magnetically stirring for 1 h for further homogenization. Prior to dip-coating, all substrates were cleaned in 50/50% solution of ethanol and acetone aided by ultrasonication for 10 min. Dip-coating was performed with a dip-coater from Ossila. The silicon (100) wafer and FTO substrates were dip-coated in a water free container with an immersion/extraction rate of 4–8 mm/s. Optimal conditions for development of a well-ordered mesoporous network were found within a relative humidity range of 10–15%. After dip-coating, the samples were directly transferred in a pre-heated furnace (Nabertherm LT3/11) at 125°C, followed by calcination to 300°C (heating rate of 5°C/min) and were hold for 12 h at this temperature stage. Subsequent calcination was accomplished by a rapid heating to 600°C (with a rate of 10°C/min) and kept at 600°C for 10 min or 12 h.

Structural characterization: The GIXRD pattern were recorded on a Rigaku SmartLab diffractometer using Cu Kα radiation ($\lambda = 0.15406$ nm). The diffractograms were measured from 10°–70° with a step size of 0.03° (in units of 2θ), having an acceleration voltage of 45 kV and current of 190 mA. The thin films thicknesses were determined by using a profilometer from Bruker (Dektak XT), having a scan rate of 6 μm/s with a stylus force of 3 mg. SEM measurements were carried out by using a Philips XL30 FEG with a voltage of 10 keV and at a working distance of 10 cm. For TEM investigations, a razor blade was used to scrape off flakes of the CFO thin films deposited on silicon substrates. 2 ml of ethanol were added to the CFO flakes and then dispersed with the help of an ultrasonic bath. The dispersion was allowed to settle for 20 sec in order to separate large particles. Three droplets of the upper part of the dispersion were applied on a carbon coated copper grid (holey type, Plano GmbH). After subsequent evaporation of the ethanol, the samples were coated with a thin carbon film (carbon coater MED 010, Bal-Tec AG, Balzers) to eliminate charging from the incident electron beam in the TEM. Investigation of the samples

were accomplished using the TEM and STEM mode in a FEG TEM (JEM2100F, JEOL Ltd.). XPS measurements were conducted normal to the surface with a SPECS PHOIBOS 150 spectrometer using a monochromatic Al Kα X-ray source (Focus 500 with XR50M (SPECS) with $hv = 1486.74$ eV) as part of the DAISY-FUN cluster tool. Survey and detail spectra were measured in fixed analyzer transmission mode with a pass energy of 20 eV (step size of 1.0 eV) and 10 eV (step size of 0.05 eV), respectively. The binding energy was calibrated by yielding the Fermi level edge of Au, Ag, Cu to 0 eV binding energy as well as $Au4f_{7/2}$ at 83.98 eV, $Ag3d_{5/2}$ at 368.26 eV and $Cu2p_{3/2}$ at 932.67 eV binding energy with deviations ≤ 50 meV.

Optical and (photo-)electrochemical characterization: The UV-Vis spectra were recorded with a Perkin Elmer lambda 900 UV/VIS/NIR spectrometer. Absorbance spectra were obtained by measuring transmittance in the wavelength range from 280–1000 nm with a sampling rate of 300 nm/min with 2 nm intervals. After converting the absorbance spectrum into a Tauc plot, the direct and indirect optical band gap of CFO thin films were determined from Tauc plot slope intersection with the baseline on x-axis. Cyclic Voltammetry (CV) measurements were recorded in a potential range of 0–1.6 V vs. RHE with a scan rate of 50 mV/s for 20 cycles. The double-layer capacitance was determined by measuring the cyclic voltammetry in the non-faradaic region within a potential window of 200 mV (1.15–1.35 V vs. RHE) using different scan rate ranging from 10–100 mV/s. The photoelectrochemical measurements were carried out by using a Zahner cell and a three-electrode setup (PECC-2 cell from Zahner Elektrik GmbH) controlled by a Zahner Zennium potentiostat (P211). The three electrode setups consisted of the CFO films deposited on FTO substrates and used as a working electrode, Hg/HgO as a reference electrode, and Pt as a counter electrode. All CFO samples were characterized in 0.1 M NaOH electrolyte with a pH value of 12.9. For the analysis with a hole scavenger, 1 M Na_2SO_3 was added to the electrolyte (pH 12.9). The chopped light voltammetry scan has been measured with white light LED having an intensity of 100 mW/cm^2 ($\lambda_{exc} = 536$ nm) within a potential range of 800–1600 mV vs. RHE (reversible hydrogen electrode) using a scan rate of 5 mV/s. Surface photovoltage spectroscopy (SPS) was conducted on CFO-coated FTO substrates, which were brought in contact with nanopurified water containing 0.02 M $NaIO_4$ and covered by a glass slip (Fisher Scientific, thickness 0.17–0.25 mm), as shown in Figure 6A. The data were collected with a vibrating gold Kelvin probe (3 mm diameter, Delta PHI Besocke) mounted inside a home-built chamber and a Kelvin control 07 (Delta PHI Besocke) possessing a sensitivity of 1 mV. With a constant sample-probe distance of ca. 1 mm the CFOs were illuminated through the probe grid with monochromatic light stemming from a 300 W Xe lamp, which was filtered through an Oriel Cornerstone 130 monochromator. Hence, the light intensity range can be considered to be 0.1–0.3 mW/cm^2. All SPV spectra were corrected for drift by subtracting the corresponding dark background.

Conflict of Interest

The authors declare no conflict of interest.

Data Availability Statement

The data that support the findings of this study are available from the corresponding author upon reasonable request.

[1] H.-O. Pörtner, D. C. Roberts, H. Adams, C. Adler, P. Aldunce, E. Ali, R. A. Begum, R. Betts, R. B. Kerr, R. Biesbroek, *IPCC Sixth Assessment Report* **2022**.

[2] M. G. Walter, E. L. Warren, J. R. McKone, S. W. Boettcher, Q. Mi, E. A. Santori, N. S. Lewis, *Chem. Rev.* **2010**, *110*, 6446.

[3] Y. He, T. Hamann, D. Wang, *Chem. Soc. Rev.* **2019**, *48*, 2182.

[4] M. D. Rashid, M. K. Al Mesfer, H. Naseem, M. Danish, *Intern. J. Eng. Adv. Technol.* **2015**.

[5] Y. J. Jang, J. S. Lee, *ChemSusChem* **2019**, *12*, 1835.

[6] A. Fujishima, K. Honda, *Nature* **1972**, *238*, 37.

[7] F. E. Osterloh, *Chem. Mater.* **2008**, *20*, 35.

[8] F. E. Osterloh, *Chem. Soc. Rev.* **2013**, *42*, 2294.

[9] K. Sivula, R. van de Krol, *Nat. Rev. Mater.* **2016**, *1*, 1.

[10] J. H. Kim, H. E. Kim, J. H. Kim, J. S. Lee, *J. Mater. Chem. A* **2020**, *8*, 9447.

[11] W. Yang, J. Moon, *ChemSusChem* **2019**, *12*, 1889.

[12] K. Sivula, F. Le Formal, M. Grätzel, *ChemSusChem* **2011**, *4*, 432.

[13] M. Einert, R. Ostermann, T. Weller, S. Zellmer, G. Garnweitner, B. M. Smarsly, R. Marschall, *J. Mater. Chem. A* **2016**, *4*, 18444.

[14] R. Siavash Moakhar, S. M. Hosseini-Hosseinabad, S. Masudy-Panah, A. Seza, M. Jalali, H. Fallah-Arani, F. Dabir, S. Gholipour, Y. Abdi, M. Bagheri-Hariri, *Adv. Mater.* **2021**, *33*, 2007285.

[15] M. Einert, T. Weller, T. Leichtweiß, B. M. Smarsly, R. Marschall, *ChemPhotoChem* **2017**, *1*, 326.

[16] I. V. Bagal, N. R. Chodankar, M. A. Hassan, A. Waseem, M. A. Johar, D.-H. Kim, S.-W. Ryu, *Int. J. Hydrogen Energy* **2019**, *44*, 21351.

[17] L. Pan, J. H. Kim, M. T. Mayer, M.-K. Son, A. Ummadisingu, J. S. Lee, A. Hagfeldt, J. Luo, M. Grätzel, *Nat. Catal.* **2018**, *1*, 412.

[18] D. K. Lee, D. Lee, M. A. Lumley, K.-S. Choi, *Chem. Soc. Rev.* **2019**, *48*, 2126.

[19] D. H. Taffa, R. Dillert, A. C. Ulpe, K. C. L. Bauerfeind, T. Bredow, D. W. Bahnemann, M. Wark, *J. Photonics Energy* **2016**, *7*, 12009.

[20] R. A. Henning, P. Uredat, C. Simon, A. Bloesser, P. Cop, M. T. Elm, R. Marschall, *J. Phys. Chem. C* **2019**, *123*, 18240.

[21] K. Kirchberg, S. Wang, L. Wang, R. Marschall, *ChemPhysChem* **2018**, *19*, 2313.

[22] X. Zhu, N. Guijarro, Y. Liu, P. Schouwink, R. A. Wells, F. Le Formal, S. Sun, C. Gao, K. Sivula, *Adv. Mater.* **2018**, *30*, 1801612.

[23] N. Guijarro, P. Bornoz, M. Prévot, X. Yu, X. Zhu, M. Johnson, X. Jeanbourquin, F. Le Formal, K. Sivula, *Sustain. Energy Fuels* **2018**, *2*, 103.

[24] M. I. Díez-García, T. Lana-Villarreal, R. Gómez, *ChemSusChem* **2016**, *9*, 1504.

[25] K. Kirchberg, R. Marschall, *Sustain. Energy Fuels* **2019**, *3*, 1150.

[26] Y. Liu, F. Le Formal, F. Boudoire, L. Yao, K. Sivula, N. Guijarro, *J. Mater. Chem. A* **2019**, *7*, 1669.

[27] S. Park, J. H. Baek, L. Zhang, J. M. Lee, K. H. Stone, I. S. Cho, J. Guo, H. S. Jung, X. Zheng, *ACS Sustainable Chem. Eng.* **2019**, *7*, 5867.

[28] S. Chen, D. Huang, P. Xu, W. Xue, L. Lei, M. Cheng, R. Wang, X. Liu, R. Deng, *J. Mater. Chem. A* **2020**, *8*, 2286.

[29] J. Kampmann, S. Betzler, H. Hajiyani, S. Häringer, M. Beetz, T. Harzer, J. Kraus, B. V. Lotsch, C. Scheu, R. Pentcheva, *Nanoscale* **2020**, *12*, 7766.

[30] A. Cots, P. Bonete, R. Gómez, *ACS Appl. Mater. Interfaces* **2018**, *10*, 26348.

[31] C. J. Brinker, Y. Lu, A. Sellinger, H. Fan, *Adv. Mater.* **1999**, *11*, 579.

[32] E. Celik, Y. Ma, T. Brezesinski, M. T. Elm, *Phys. Chem. Chem. Phys.* **2021**, *23*, 10706.

[33] D. Grosso, C. Boissière, B. Smarsly, T. Brezesinski, N. Pinna, P. A. Albouy, H. Amenitsch, M. Antonietti, C. Sanchez, *Nat. Mater.* **2004**, *3*, 787.

[34] E. Ortel, A. Fischer, L. Chuenchom, J. Polte, F. Emmerling, B. Smarsly, R. Kraehnert, *Small* **2012**, *8*, 298.

[35] B. Smarsly, M. Antonietti, *Eur. J. Inorg. Chem.* **2006**, *2006*, 1111.

[36] J. Yue, C. Suchomski, T. Brezesinski, B. M. Smarsly, *ChemNanoMat* **2015**, *1*, 415.

[37] T. Brezesinski, J. Wang, J. Polleux, B. Dunn, S. H. Tolbert, *J. Am. Chem. Soc.* **2009**, *131*, 1802.

[38] M. Einert, M. Mellin, N. Bahadorani, C. Dietz, S. Lauterbach, J. P. Hofmann, *ACS Appl. Energ. Mater.* **2022**, *5*, 717.

[39] B. Smarsly, M. Antonietti, *Eur. J. Inorg. Chem.* **2006**, *2006*, 1111.

[40] A. Thomas, H. Schlaad, B. Smarsly, M. Antonietti, *Langmuir* **2003**, *19*, 4455.

[41] C. Reitz, C. Suchomski, J. Haetge, T. Leichtweiss, Z. Jagličić, I. Djerdj, T. Brezesinski, *Chem. Commun.* **2012**, *48*, 4471.

[42] C. Reitz, C. Suchomski, V. S. K. Chakravadhanula, I. Djerdj, Z. Jagličić, T. Brezesinski, *Inorg. Chem.* **2013**, *52*, 3744.

[43] T. E. Quickel, H. van Le, T. Brezesinski, S. H. Tolbert, *Nano Lett.* **2010**, *10*, 2982.

[44] J. Haetge, C. Suchomski, T. Brezesinski, *Inorg. Chem.* **2010**, *49*, 11619.

[45] L. A. Dubraja, C. Reitz, L. Velasco, R. Witte, R. Kruk, H. Hahn, T. Brezesinski, *ACS Appl. Nano Mater.* **2017**, *1*, 65.

[46] J.-M. Wu, I. Djerdj, T. von Graberg, B. M. Smarsly, *Beilstein J. Nanotechnol.* **2012**, *3*, 123.

[47] M. Einert, A. Waheed, S. Lauterbach, M. Mellin, M. Rohnke, L. Q. Wagner, J. Gallenberger, C. Tian, B. M. Smarsly, W. Jaegermann, F. Hess, H. Schlaad, J. P. Hofmann, *Small* **2023**, n/a, 2205412.

[48] D. Chandra, K. Saito, T. Yui, M. Yagi, *Angew. Chem.* **2013**, *125*, 12838.

[49] D. Chandra, K. Saito, T. Yui, M. Yagi, *ACS Sustainable Chem. Eng.* **2018**, *6*, 16838.

[50] B. Eckhardt, E. Ortel, D. Bernsmeier, J. Polte, P. Strasser, U. Vainio, F. Emmerling, R. Kraehnert, *Chemis. Mater.* **2013**, *25*, 2749.

[51] P. Hartmann, D.-K. Lee, B. M. Smarsly, J. Janek, *ACS Nano* **2010**, *4*, 3147.

[52] T. von Graberg, P. Hartmann, A. Rein, S. Gross, B. Seelandt, C. Röger, R. Zieba, A. Traut, M. Wark, J. Janek, *Sci. Technol. Adv. Mater.* **2011**.

[53] K. Brezesinski, J. Haetge, J. Wang, S. Mascotto, C. Reitz, A. Rein, S. H. Tolbert, J. Perlich, B. Dunn, T. Brezesinski, *Small* **2011**, *7*, 407.

[54] J. La Calvo-de Rosa, M. Segarra, *ACS Omega* **2019**, *4*, 18289.

[55] M. Schröder, S. Sallard, M. Böhm, M. Einert, C. Suchomski, B. M. Smarsly, S. Mutisya, M. F. Bertino, *Small* **2014**, *10*, 1566.

[56] M. Einert, P. Hartmann, B. Smarsly, T. Brezesinski, *Sci. Rep.* **2021**, *11*, 1.

[57] M. Schröder, S. Sallard, M. Böhm, M. Einert, C. Suchomski, B. M. Smarsly, S. Mutisya, M. F. Bertino, *Small* **2014**, *10*, 1566.

[58] C. Suchomski, D. J. Weber, P. Dolcet, A. Hofmann, P. Voepel, J. Yue, M. Einert, M. Möller, S. Werner, S. Gross, *J. Mater. Chem. A* **2017**, *5*, 16296.

[59] C. C. L. McCrory, S. Jung, J. C. Peters, T. F. Jaramillo, *J. Am. Chem. Soc.* **2013**, *135*, 16977.

[60] M. C. Biesinger, B. P. Payne, A. P. Grosvenor, L. W. M. Lau, A. R. Gerson, R. S. C. Smart, *Appl. Surf. Sci.* **2011**, *257*, 2717.

[61] P. C. J. Graat, M. A. J. Somers, *Appl. Surf. Sci.* **1996**, *100*, 36.

[62] M. Einert, M. Mellin, N. Bahadorani, C. Dietz, S. Lauterbach, J. P. Hofmann, *ACS Appl. Energ. Mater.* **2022**, *5*, 717.

[63] P. W. Menezes, A. Indra, A. Bergmann, P. Chernev, C. Walter, H. Dau, P. Strasser, M. Driess, *J. Mater. Chem. A* **2016**, *4*, 10014.

[64] M. Einert, C. Wessel, F. Badaczewski, T. Leichtweiß, C. Eufinger, J. Janek, J. Yuan, M. Antonietti, B. M. Smarsly, *Macromol. Chem. Phys.* **2015**, *216*, 1930.

[65] K. Brezesinski, J. Wang, J. Haetge, C. Reitz, S. O. Steinmueller, S. H. Tolbert, B. M. Smarsly, B. Dunn, T. Brezesinski, *J. Am. Chem. Soc.* **2010**, *132*, 6982.

[66] R. Dillert, D. H. Taffa, M. Wark, T. Bredow, D. W. Bahnemann, *APL Mater.* **2015**, *3*, 104001.

[67] M. Pourbaix, *NACE* **1974**, *307*.

[68] E. M. Elsayed, M. M. Rashad, H. F. Khalil, I. A. Ibrahim, Hussein, M. M. El-Sabbah, *Appl. Nanosci.* **2016**, *6*, 485.

[69] C. A. Mesa, L. Francas, K. R. Yang, P. Garrido-Barros, E. Pastor, Y. Ma, A. Kafizas, T. E. Rosser, M. T. Mayer, E. Reisner, *Nat. Chem.* **2020**, *12*, 82.

[70] L. M. Peter, *J. Solid State Electrochem.* **2013**, *17*, 315.

[71] H. K. Dunn, J. M. Feckl, A. Müller, D. Fattakhova-Rohlfing, S. G. Morehead, J. Roos, L. M. Peter, C. Scheu, T. Bein, *Phys. Chem. Chem. Phys.* **2014**, *16*, 24610.

[72] E. A. Ponomarev, L. M. Peter, *J. Electroanal. Chem.* **1995**, *396*, 219.

[73] J. Krüger, R. Plass, M. Grätzel, P. J. Cameron, L. M. Peter, *J. Phys. Chem. B* **2003**, *107*, 7536.

[74] J. E. Thorne, J.-W. Jang, E. Y. Liu, D. Wang, *Chem. Sci.* **2016**, *7*, 3347.

[75] C. Zachäus, F. F. Abdi, L. M. Peter, R. van de Krol, *Chem. Sci.* **2017**, *8*, 3712.

[76] Y. Liu, F. Le Formal, F. Boudoire, N. Guijarro, *ACS Appl. Energ. Mater.* **2019**, *2*, 6825.

[77] L. M. Peter, E. A. Ponomarev, D. J. Fermin, *J. Electroanal. Chem.* **1997**, *427*, 79.

[78] F. E. Osterloh, *ACS Energy Lett.* **2017**, *2*, 445.

[79] Y. Yang, J. Wang, J. Zhao, B. A. Nail, X. Yuan, Y. Guo, F. E. Osterloh, *ACS Appl. Mater. Interfaces* **2015**, *7*, 5959.

[80] J. Zhao, B. A. Nail, M. A. Holmes, F. E. Osterloh, *J. Phys. Chem. Lett.* **2016**, *7*, 3335.

[81] T. L. Shelton, N. Harvey, J. Wang, F. E. Osterloh, *Appl. Catal. A* **2016**, *521*, 168.

[82] X. Ma, X. Cui, Z. Zhao, M. A. Melo, E. J. Roberts, F. E. Osterloh, *J. Mater. Chem. A* **2018**, *6*, 5774.

[83] L. Kronik, Y. Shapira, *Surface Sci. Rep.* **1999**, *37*, 1.

[84] B. J. Trześniewski, W. A. Smith, *J. Mater. Chem. A* **2016**, *4*, 2919.

[85] J. Zhao, F. E. Osterloh, *J. Phys. Chem. Lett.* **2014**, *5*, 782.

[86] Y. Cheng, C. Xiao, B. Mahmoudi, R. Scheer, A. W. Maijenburg, F. E. Osterloh, *EES Catalysis* **2023**, *1*, 74-83.

[87] P. Vany`sek, Lide, *CRC handbook of chemistry and physics* **2008**.

[88] S. Bastide, D. Gal, D. Cahen, L. Kronik, *Rev. Sci. Instrum.* **1999**, *70*, 4032.

[89] L. V. Keldysh, *Soviet J. Experim. Theor. Phys. Lett.* **1979**, *29*, 658.

[90] X. Chen, K. Wang, M. C. Beard, *Phys. Chem. Chem. Phys.* **2019**, *21*, 16399.

[91] W. Z. Franz, *Naturforsch. A* **1958**, *13*, 484.

[92] Cheng, Y. C. Xiao, B. Mahmoudi, R. Scheer, A. W. Maijenburg, F. E. Osterloh, *EES Catalysis* **2022**, *1*, 74–83.

[93] R. M. Doughty, B. Hodges, J. Dominguez, R. Han, Z. Zhao, S. Assavachin, F. E. Osterloh, *J. Phys. Chem. C* **2020**, *124*, 18426.

[94] B. Klahr, S. Gimenez, F. Fabregat-Santiago, T. Hamann, J. Bisquert, *J. Am. Chem. Soc.* **2012**, *134*, 4294.

[95] Y. Xu, F. Zhang, T. Sheng, T. Ye, D. Yi, Y. Yang, S. Liu, X. Wang, J. Yao, *J. Mater. Chem. A* **2019**, *7*, 23191.

[96] R. Ovcharenko, E. Voloshina, J. Sauer, *Phys. Chem. Chem. Phys.* **2016**, *18*, 25560.

[97] M.-T. Nguyen, S. Piccinin, N. Seriani, R. Gebauer, *ACS Catal.* **2015**, *5*, 715.

[98] I. Ahmed, L. Shi, H. Pasanen, P. Vivo, P. Maity, M. Hatamvand, Y. Zhan, *Light: Science & Applications* **2021**, *10*, 1.

[99] B. Yang, K. Han, *Acc. Chem. Res.* **2019**, *52*, 3188.

[100] A. Polo, F. Boudoire, C. R. Lhermitte, Y. Liu, N. Guijarro, M. V. Dozzi, E. Selli, K. Sivula, *J. Mater. Chem. A* **2021**, *9*, 27736.